Single-Sensor RGB-NIR Imaging: High-Quality System Design and Prototype Implementation

Yusuke Monno, *Member, IEEE,* Hayato Teranaka, Kazunori Yoshizaki, Masayuki Tanaka, *Member, IEEE,* and Masatoshi Okutomi, *Member, IEEE*

Abstract—In recent years, many applications using a set of red-green-blue (RGB) and near-infrared (NIR) images, also called an RGB-NIR image, have been proposed. However, RGB-NIR imaging, i.e., simultaneous acquisition of RGB and NIR images, is still a laborious task because existing acquisition systems typically require two sensors or shots. In contrast, single-sensor RGB-NIR imaging using an RGB-NIR sensor, which is composed of a mosaic of RGB and NIR pixels, provides a practical and low-cost way of one-shot RGB-NIR image acquisition. In this paper, we investigate high-quality system designs for single-sensor RGB-NIR imaging. We first present a system evaluation framework using a new hyperspectral image dataset we constructed. Different from existing work, our framework takes both the RGB-NIR sensor characteristics and the RGB-NIR imaging pipeline into account. Based on the evaluation framework, we then design each imaging factor that affects the RGB-NIR imaging quality and propose the best-performed system design. We finally present the configuration of our developed prototype RGB-NIR camera, which was implemented based on the best system design, and demonstrate several potential applications using the prototype.

Index Terms—Image sensor, imaging pipeline, filter array pattern, demosaicking, color correction, RGB, near-infrared (NIR).
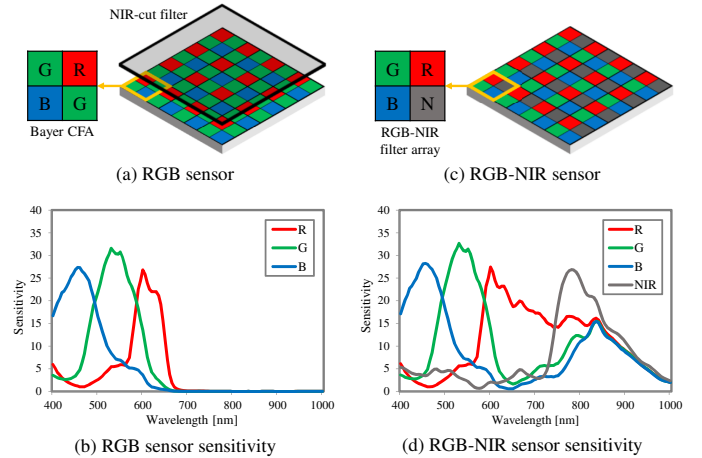

Fig. 1. Image sensors and their sensitivity: (a) RGB sensor, (b) RGB sensor sensitivity, (c) RGB-NIR sensor, and (d) RGB-NIR sensor sensitivity.

I. INTRODUCTION

IN recent years, many applications using a set of red-green-blue (RGB) and near-infrared (NIR) images, also called an RGB-NIR image, have been proposed. Different spectral properties between RGB and NIR images offer useful information for various applications such as image restoration [1], image enhancement [2]–[4], image fusion [5], [6], dehazing [7], [8], scene categorization [9], face recognition [10], shadow detection [11], and heart rate measurement [12]. However, simultaneous acquisition of RGB and NIR images, also termed RGB-NIR imaging, is still a laborious task because existing acquisition systems typically require two sensors [2], [3] or

Y. Monno, H. Teranaka, M. Tanaka, and M. Okutomi are with the Department of Systems and Control Engineering, School of Engineering, Tokyo Institute of Technology, Meguro-ku, Tokyo 152-8550, Japan (e-mail: ymonno@ok.sc.e.titech.ac.jp; hteranaka@ok.ctrl.titech.ac.jp; mtanaka@sc.e.titech.ac.jp; mxo@sc.e.titech.ac.jp).

M. Tanaka is also with Artificial Intelligence Research Center, National Institute of Advanced Industrial Science and Technology, Koto-ku, Tokyo 135-0064, Japan.

K. Yoshizaki is with Olympus Corporation, Hachioji, Tokyo 192-8512, Japan (e-mail: kazunori_yoshizaki@ot.olympus.co.jp).

two shots [9], [11], where one is required for RGB and the other is required for NIR. The necessity of two sensors or shots also makes the systems large, expensive, and complicated.

In current color digital cameras, single-senor RGB imaging using the Bayer color filter array (CFA) [13] (see Fig. 1(a)) is well established [14]. An image sensor equipped with the Bayer CFA records only one pixel value among RGB values at each pixel. The other two missing pixel values are estimated from the recorded mosaic data of RGB values by an interpolation process called demosaicking (or demosaicing) [15], [16]. The combination of the Bayer CFA and the demosaicking process enables one-shot acquisition of the RGB image using only a single image sensor, and hence reduces the size and cost of the camera.

The one-shot, compact and low-cost properties of the single-sensor RGB imaging are also desirable for RGB-NIR imaging. Therefore, the extension of the single-sensor RGB imaging to single-sensor RGB-NIR imaging has received increasing attention [17]–[22]. This extension can be realized by developing an RGB-NIR sensor that is an image sensor equipped with an RGB-NIR filter array (see Fig. 1(c) for an example). The RGB-NIR sensor offers a practical way of one-shot RGB-NIR imaging, without increased size and cost from current color digital cameras.

Similar to conventional RGB sensors with the Bayer CFA, the raw output of an RGB-NIR sensor is mosaic data of R, G, B, and NIR values. Therefore, to obtain the RGB and the NIR images in a desired output format, the mosaic data must be processed through an imaging pipeline. As a consequence,

the RGB-NIR imaging quality is affected by both the RGB-NIR sensor characteristics, such as a filter array pattern (FAP) and spectral sensitivity, and the RGB-NIR imaging pipeline converting the mosaic data to the output RGB and NIR images. However, existing research on single-sensor RGB-NIR imaging mainly focuses on either sensor characterization [17], [18] or image reconstruction methodology [19]–[22]. In addition, to the best of our knowledge, there is no existing work that systematically evaluates different sensor and imaging pipeline designs for high-quality single-sensor RGB-NIR imaging.

In this paper, our purpose is to propose high-quality system designs for single-sensor RGB-NIR imaging by taking both the sensor characteristics and the imaging pipeline into account. Specifically, we investigate the following imaging factors that affect the RGB-NIR imaging quality.

RGB-NIR FAPs and demosaicking algorithms are core factors of single-sensor RGB-NIR imaging systems. Although the 2×2 RGB-NIR FAP in Fig. 1(c) is commonly adopted (e.g., [19]–[24]), there are few comparative studies of different RGB-NIR FAPs. In this work, we propose two RGB-NIR FAPs and compare them with the common 2×2 RGB-NIR FAP. We also propose a demosaicking framework for our FAPs using state-of-the-art residual interpolation [25].

Color correction is particularly important for single-sensor RGB-NIR imaging. As shown in Fig. 1(d), typical RGB filters have spectral sensitivity in the NIR domain. These phenomena are refereed to as spectral crosstalks [21], [22]. For current RGB sensors, an NIR-cut filter is placed in front of the sensor (see Fig. 1(a)) to avoid undesirable effects of the spectral crosstalks for color representation. However, the NIR-cut filter needs to be removed for single-sensor RGB-NIR imaging, resulting in severe color shifts of the acquired RGB image. Figure 2 shows examples of the color shift for the color chart. The RGB image of the RGB-NIR sensor in Fig. 2(b) is more reddish and less color saturated than that of the RGB sensor in Fig. 2(a). The role of color correction is to correct such color shifts and reproduce the image with desired color representation, typically in the sRGB color space as shown in Fig. 2(c). In this work, we evaluate standard least-squares color correction algorithms [26]–[28] for single-sensor RGB-NIR imaging. We also propose an effective refinement process to suppress demosaicking error amplification by color correction.

Spectral sensitivity is another important factor that affects the color fidelity of the acquired RGB image and the spectral property of the acquired NIR image. However, spectral sensitivity of manufacturable RGB-NIR sensors is physically and technically limited. One feasible option to customize the spectral sensitivity is to place an optical filter in front of the sensor or lens. In this work, we maximize the RGB-NIR imaging quality by investigating an optimal optical filter.

To design a high-quality single-sensor RGB-NIR imaging system, it is important to evaluate the above-mentioned factors considering the overall system performance. Therefore, in this paper, we first construct a system evaluation framework. For the evaluation, we use our new hyperspectral image dataset that covers the spectral range from 420nm to 1000nm. We then propose the best-performed system design by properly designing each imaging factor based on the evaluation framework.

(a) RGB of the RGB sensor in Fig. 1(b)   (b) RGB of the RGB-NIR sensor in Fig. 1(d)   (c) sRGB
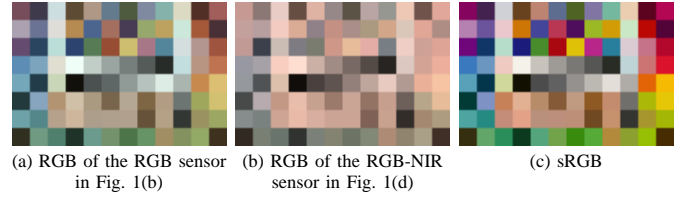
Fig. 2. Simulated color chart images: (a) RGB of the RGB sensor, (b) RGB of the RGB-NIR sensor, and (c) sRGB. Daylight is used for simulating (a) and (b). The image (b) is more reddish and less color saturated than the image (a) due to the spectral crosstalks of the RGB-NIR sensor.

We finally validate the realizability of the best system design by our developed prototype RGB-NIR camera. Contributions of this paper are summarized as follows.

- We construct a system evaluation framework for single-sensor RGB-NIR imaging. Our evaluation framework takes both the RGB-NIR sensor characteristics and the RGB-NIR imaging pipeline into account. A part of the dataset images and sample codes to reproduce the framework is publicly available at our website[1].
- Based on the evaluation framework, we propose high-quality system designs for single-sensor RGB-NIR imaging. We demonstrate that our proposed RGB-NIR FAP called the "dense-NIR FAP" provides the best performance among compared three RGB-NIR FAPs.
- We validate the realizability of the best system design, which is based on our dense-NIR FAP, by our developed prototype RGB-NIR camera that operates in real time. We demonstrate several potential applications using the prototype camera.

This paper is an extended version of our conference papers [29]–[31], in which we have proposed two RGB-NIR FAPs, demosaicking frameworks for the FAPs, and a color correction refinement process for RGB-NIR sensors. In this paper, we combine all these proposals, with more dedicated discussion and experiments for high-quality system designs, and present a new content of the spectral sensitivity design. We also present the configuration of our newly developed prototype RGB-NIR camera and several applications using the prototype, while the conference papers only contain simulation results.

The rest of this paper is organized as follows. Section II briefly reviews related work. Section III presents our system evaluation framework and proposed high-quality system designs. Section IV presents the configuration and the applications of our developed prototype RGB-NIR camera. Section V concludes the paper and presents future work.

II. RELATED WORK

A. RGB-NIR FAPs and demosaicking algorithms

Existing work (e.g., [19]–[24]) commonly adopts the 2×2 RGB-NIR FAP of Fig. 3(b), where half of the G filters in the Bayer FAP (see Fig. 3(a)) are replaced with the NIR filters. In other words, all spectral bands are uniformly sampled. In what follows, we refer to this FAP as the uniform FAP. A few literatures have presented a demosaicking algorithm for the

---

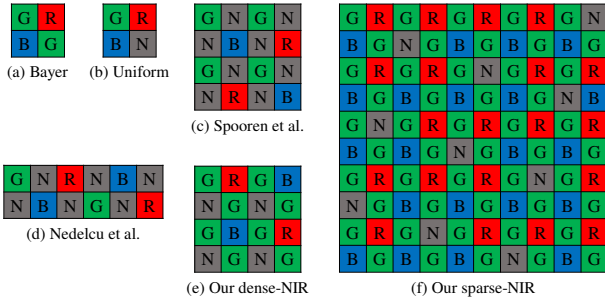[1]http://www.ok.sc.e.titech.ac.jp/res/MSI/SENJ-RGB-NIR.html

Fig. 3. Different FAPs: (a) The Bayer FAP [13], (b) the uniform FAP [19]–[24], (c) the Spooren et al. FAP [17], (d) the Nedelcu et al. FAP [32], (e) our dense-NIR FAP, and (f) our sparse-NIR FAP.

TABLE I
SAMPLING DENSITY OF EACH BAND IN DIFFERENT FAPS.

FAP	Size	R	G	B	NIR
Bayer	2×2	1/4	1/2	1/4	–
Uniform	2×2	1/4	1/4	1/4	1/4
Our dense-NIR	4×4	1/8	1/2	1/8	1/4
Our sparse-NIR	10×10	1/5	1/2	1/5	1/10
Spooren [17]	4×4	1/8	1/4	1/8	1/2
Nedelcu [32]	2×6	1/6	1/6	1/6	1/2
Lu [33]	4×4	Use specialized filters			
Sadeghipoor [34]	4×4	Use specialized filters			

uniform FAP in detail [20]–[22]. Martinello et al. proposed an interpolation-based algorithm that can effectively incorporate an existing high-quality Bayer demosaicking algorithm for the RGB image reconstruction [20]. Tang et al. modeled the demosaicking process as an optimization problem and solved it with image regularization functions [21]. Hu et al. recently improved the Tang et al. algorithm using convolutional sparse cording to solve the optimization problem [22]. Although the optimization-based approaches [21], [22] offer higher performance, they require higher computational cost (e.g., more than 8 minutes for a 380×336 pixel image, as reported in [22]).

As other RGB-NIR FAPs, Spooren et al. proposed a 4×4 FAP of Fig. 3(c) [17] and Nedelcu et al. proposed a 2×6 FAP of Fig. 3(d) [32], respectively. In these FAPs, half of the pixels are the NIR pixels, and thus the NIR imaging is the main target. The demosaicking algorithms for these FAPs have not described in detail in [17], [32]. Lu et al. and Sadeghipoor et al. proposed several frameworks that jointly solve the FAP design and the demosaicking problems [33]–[35]. Although these frameworks theoretically work well, manufacturing of the resultant sensors are technically difficult due to the necessity of the specialized spectral filters.

In this work, considering the reproducibility of the state-of-the-art demosaicking algorithm and the feasibility of hardware implementation, we consider the most common uniform FAP in our system design. We also propose two RGB-NIR FAPs, as shown in Fig. 3(e) and 3(f), and compare them with the uniform FAP. Table I summarizes the sampling density of each band in the above-mentioned FAPs.

B. Color correction algorithms

Color correction is a process that transforms a camera-specific color space into a standard or a desired color space,

typically the XYZ or the sRGB color space [36], [37]. For conventional RGB sensors, least-squares algorithms, such as linear color correction (LCC) [26], polynomial color correction (PCC) [27], and root-polynomial color correction (RPCC) [28], are the most widely used algorithms. The least-squares algorithms can be extended for the RGB-NIR sensors [19], [38]. There are several algorithms that are designed for the RGB-NIR sensors, such as based on spectral decomposition [39], sparse representation [40], and neural networks [41], [42]. Tang et al. and Hu et al. jointly solved the demosaicking and the color correction problems as the optimization framework [21], [22]. However, these algorithms generally require higher computational cost and memory than the least-squares algorithms.

In this work, we evaluate hardware-efficient least-squares algorithms, i.e., LCC, PCC, and RPCC, for our system design. We also propose an effective refinement process to suppress demosaicking error amplification, which is a new challenge of color correction for the RGB-NIR sensors.

C. Spectral sensitivity

Some research groups have analyzed manufacturable spectral sensitivity for the RGB-NIR sensors, based on their own technology such as the gated CMOS sensor [17], the pixel-level integration of the NIR-cut filter [18], the transverse field detector [43], the monolithically integrating interference filters [44], and the thin film deposition and etching [45].

In this work, we developed a prototype RGB-NIR camera with the spectral sensitivity shown in Fig 1(d), which was manufacturable by our technology. Since the spectral sensitivity of manufacturable sensors is physically and technically limited, we introduce an optical notch filter in front of the lens to improve the RGB-NIR imaging quality. Although the integration of the notch filter is implicitly performed in some existing work (e.g., [21]), we explicitly optimize the cut-off wavelengths of the notch filter.

III. PROPOSED HIGH-QUALITY SYSTEM DESIGNS

A. Hyperspectral image dataset

We start with the description of our constructed hyperspectral image dataset, which was used for our system evaluation. We used a monochrome camera and two VariSpec tunable filters [46], VIS for 420-650nm and SNIR for 650-1000nm, for capturing each hyperspectral image. The captured hyperspectral image consists of a set of narrow-band images from 420nm to 1000nm at every 10nm intervals. The hyperspectral image was then converted into a form of spectral reflectance by a calibration process using a colorchecker whose spectral reflectance property is known. The dataset contains 40 scenes with cropped 512×512 pixels, as shown in Fig. 4

B. System evaluation framework

Figure 5 shows the overview of our system evaluation framework. The input of the framework is hyperspectral reflectance data as explained above. As the illumination source,
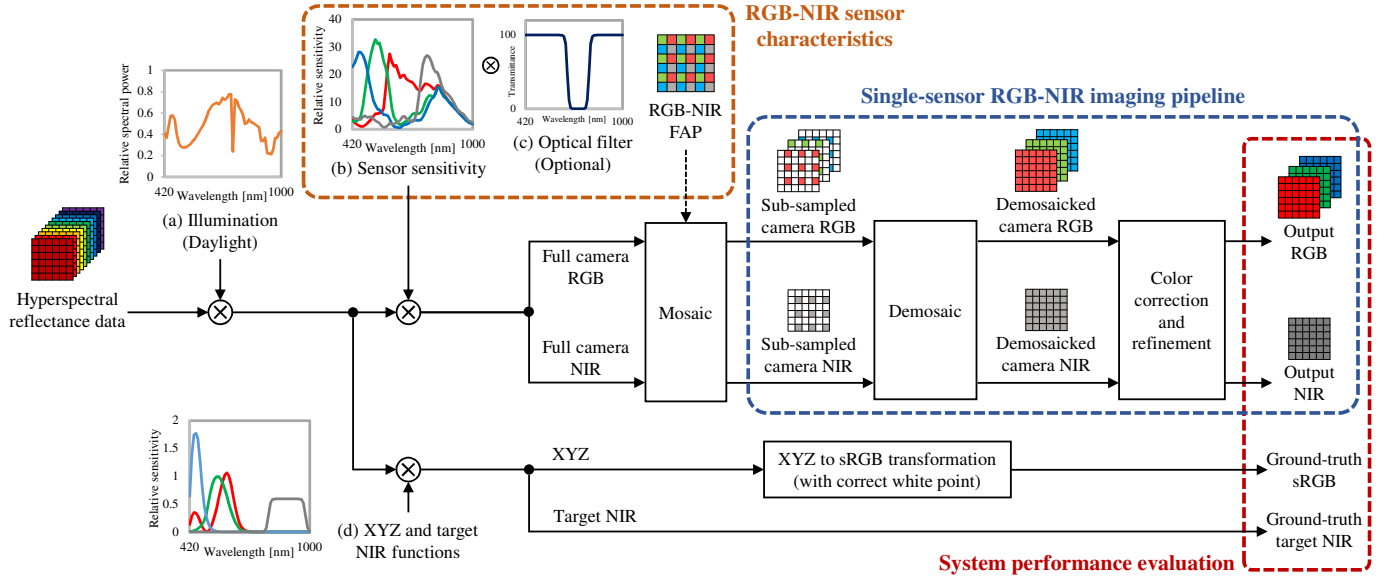
Fig. 5. Overview of our system evaluation framework using the hyperspectral image dataset.
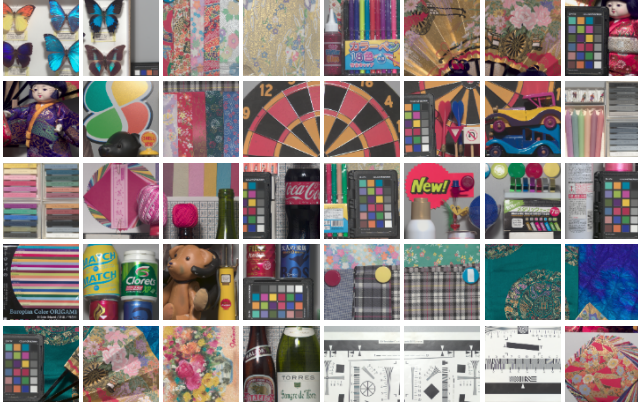

Fig. 4. Forty scenes in our hyperspectral image dataset.

we assume daylight, which has broad spectral power distribution in both visible and NIR domains. The spectral distribution of daylight was measured using a spectrometer (see Fig. 5(a)).

The lower part of Fig. 5 shows the generation process of ground-truth images. For the RGB imaging, we set the sRGB color space as our target color space. To generate the ground-truth sRGB image, the hyperspectral reflectance data is firstly converted to the XYZ image using the XYZ color matching functions (red, green, and blue lines in Fig. 5(d)). Then, the ground-truth sRGB image is generated by the XYZ-to-sRGB transformation matrix calculated using the white point of the daylight. For the NIR imaging, we also assume a target NIR space without spectral crosstalks between the visible and the NIR domains. Although the target NIR spectral range depends on applications, without loss of generality, we set the spectral range from 800nm to 1000nm as our target NIR space. The target NIR sensitivity function is shown as the gray line in Fig. 5(d). The relative sensitivity of the target NIR function is normalized to have the same area with the Y functions, i.e., the green line in Fig. 5(d). The ground-truth target NIR image is directly generated from the hyperspectral reflectance data

using the target NIR function.

The upper part of Fig. 5 shows the simulation flow of the single-sensor RGB-NIR imaging system. Firstly, full camera RGB and NIR images are generated using the spectral sensitivity functions of the RGB-NIR sensor (see Fig. 5(b)). As an option, the spectral sensitivity can be modified using an optical filter, which is placed in front of the lens. The full camera RGB and NIR images are then sub-sampled according to the RGB-NIR FAP of the sensor. The sub-sampled R, G, B, and NIR images are then interpolated by the demosaicking process. The demosaicked camera RGB and NIR images with the spectral crosstalks are finally converted to the output images in the target sRGB and NIR spaces by the color correction and refinement processes. In the performance evaluation, the output RGB and NIR images generated by the system are compared with the ground-truth sRGB and target NIR images (see the red dashed box in Fig. 5). We evaluate peak signal-to-noise ratio (PSNR) of each band and multispectral PSNR (MPSNR), which is calculated as below.

$$\text{MPSNR} = 10 \cdot \log \frac{255^2}{\frac{1}{4M} \sum_{i=1}^{4} \sum_{j=1}^{M} ||\hat{x}_{ij} - x_{ij}||_2^2}, \quad (1)$$

where M is the total number of pixels, $\hat{x}_{ij}$ is the estimated pixel value at the j-th pixel in the i-th band, where $i = \{R, G, B, NIR\}$, and x_{ij} is the corresponding ground-truth pixel value. MPSNR evaluates the overall imaging quality of the RGB-NIR imaging system.

In the following subsections, we propose high-quality system designs by considering both the RGB-NIR characteristics (the orange dashed box in Fig. 5) and the single-sensor RGB-NIR imaging pipeline (the purple dashed box in Fig. 5). Specifically, we design RGB-NIR FAPs and demosaicking algorithms in subsection III-C, evaluate least-squares color correction algorithms in subsection III-D, propose an effective color correction refinement algorithm in subsection III-E, and introduce an optimal notch filter, as shown in Fig. 5(c), in subsection III-F.
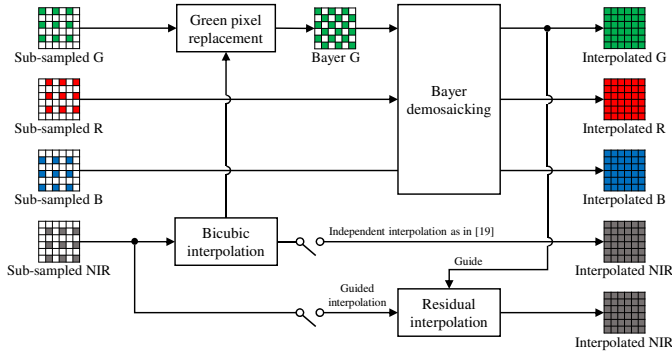
Fig. 6. The demosaicking framework of [20] for the uniform FAP.

Fig. 7. Our proposed demosaicking framework for the dense-NIR FAP. The same framework can be applied to the sparse-NIR FAP.

C. RGB-NIR FAPs and demosaicking algorithms

1) Considered FAPs: We consider the common uniform FAP and two proposed FAPs. Figure 3(c) and 3(d) show our proposed FAPs. The feature of our FAPs is that the G filters are sampled in the same density as that of the Bayer FAP. Motivated by state-of-the-art Bayer demosaicking algorithms, we later propose a demosaicking framework that effectively exploits the high sampling density of the G band. The two FAPs are discriminated by the sampling density of the NIR filters. The FAP of Fig. 3(c) samples the NIR filters in the density of 1/4, while the FAP of Fig. 3(d) samples them in the density of 1/10. In what follows, we refer to the first FAP as the dense-NIR FAP, and the second FAP as the sparse-NIR FAP, respectively. We next describe the demosaicking frameworks for the considered FAPs.

2) Demosaicking framework for the uniform FAP: Since our goal is to realize a real-time system, we adopt the computationally efficient interpolation-based algorithm by Martinello et al. [20] for the uniform FAP. Figure 6 shows the demosaicking framework of [20]. The algorithm first interpolates the sub-sampled NIR by bicubic interpolation. Then, the algorithm estimates the missing G pixel values at the NIR pixels by interpolating the G−NIR components. This process is called green pixel replacement in [20]. As the consequence of the green pixel replacement, the Bayer mosaic image is acquired. Therefore, an existing Bayer demosaicking algorithm can be applied to reconstruct the RGB image. We apply the residual interpolation (RI)-based algorithm [25], which is one of the state-of-the-arts. For the NIR image reconstruction, we consider two approaches. The first one is independent interpolation that directly uses the interpolated NIR image by bicubic interpolation as the output. The second one is guided interpolation that uses the interpolated G image as the guide for interpolating the sub-sampled NIR, assuming the spectral correlation between the G and the NIR bands. Although only the first approach is taken in [20], we also consider the second approach because it is known that the visible and the NIR images generally have correlation to some extent. We apply the RI [25] for the guided interpolation in the second approach.

3) Demosaicking framework for the dense-NIR and the sparse-NIR FAPs: Figure 7 shows the demosaicking framework of our proposed algorithm for the dense-NIR FAP. The algorithm first interpolates the most dense G band by the RI-based algorithm [47]. The algorithm then interpolates the R
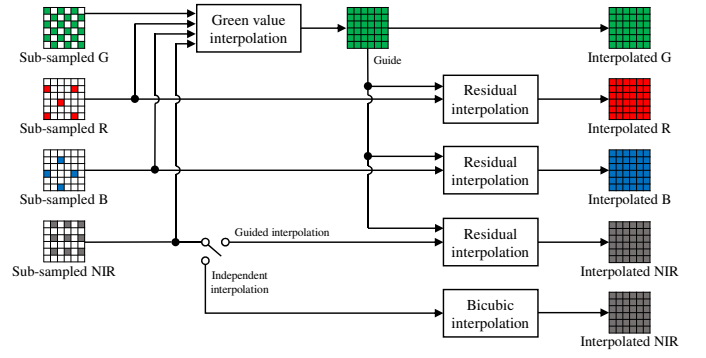
TABLE II
PERFORMANCE EVALUATION OF THE DEMOSAICKING ALGORITHMS.
AVERAGE PSNR AND MPSNR OF ALL 40 SCENES ARE PRESENTED. THE
BOLD TYPEFACE REPRESENTS THE BEST MPSNR FOR EACH FAP.

FAP	NIR Rec.	R	G	B	NIR	MPSNR
Uniform	Indep.	39.15	42.86	45.28	36.14	39.44
	Guided				42.00	**41.66**
Dense-NIR	Indep.	38.62	46.03	44.82	36.14	39.46
	Guided				43.47	**42.17**
Sparse-NIR	Indep.	40.20	47.68	47.05	30.88	36.18
	Guided				40.65	**42.59**

and the B bands by exploiting the interpolated G image as the guide for RI. The above-mentioned two approaches are taken for the NIR image reconstruction. The same demosaicking framework can be applied to the sparse-NIR FAP, which also has the high sampling density of the G band.

4) Performance evaluation: Table II summarizes the demosaicking performance. Here, to evaluate pure demosaicking performance regardless of color correction, the full "camera" RGB and NIR images without mosaicking (see Fig. 5) were used as the ground truths for calculating PSNR and MPSNR. The second column in Table II represents the used approach for the NIR image reconstruction (NIR Recon.). The approach "Indep." represents the independent interpolation, while the approach "Guided" represents the guided interpolation.

As shown in Table II, for the RGB image reconstruction, the sparse-NIR FAP offers the best performance. This is reasonable because the sparse-NIR FAP assigns more pixels to the RGB filters than the other two FAPs. For the NIR image reconstruction, the guided interpolation works much better than the independent interpolation. This is because, for many of objects in our dataset, the G and the NIR images share the edge and texture locations, even if there are intensity differences, due to the spectral sensitivity overlaps between the G and the NIR bands in our RGB-NIR sensor. In what follows, we adopt the guided interpolation for the NIR image reconstruction.

D. Color correction algorithms

We next evaluate standard least-squares color correction algorithms [26]–[28] for single-sensor RGB-NIR imaging.

TABLE III
PERFORMANCE EVALUATION OF THE COLOR CORRECTION ALGORITHMS. AVERAGE PSNR AND MPSNR OF ALL 40 SCENES ARE PRESENTED. THE BOLD TYPEFACE REPRESENTS THE BEST MPSNR FOR EACH FAP.

FAP	Model	R	G	B	NIR	MPSNR
Uniform	No CC	20.11	19.66	20.58	14.70	17.68
	LCC	29.94	29.07	31.92	26.01	28.47
	PCC	29.51	28.90	31.99	26.74	28.65
	RPCC	29.79	28.94	32.15	27.37	**28.85**
Dense-NIR	No CC	20.12	19.72	20.58	14.71	17.69
	LCC	29.00	32.80	30.56	26.09	28.74
	PCC	28.58	32.38	30.74	26.88	28.93
	RPCC	29.10	32.46	30.80	27.38	**29.16**
Sparse-NIR	No CC	20.16	19.73	20.60	14.73	17.70
	LCC	28.63	33.01	29.82	24.45	27.79
	PCC	28.17	32.63	30.03	25.17	28.04
	RPCC	28.51	32.81	30.33	25.82	**28.38**

1) General formulation: The least-squares algorithms for the RGB-NIR sensors can generally be formulated as

$$\mathbf{q} = \mathbf{M}\mathbf{p}, \tag{2}$$

where $\mathbf{q} = [r', g', b', n']^T$ represents the output color-corrected RGB and NIR values, $\mathbf{p} \in \mathbb{R}^N$ is an input vector formed by camera RGB values, and $\mathbf{M} \in \mathbb{R}^{4 \times N}$ is the color correction matrix. The elements and the dimension of the input vector $\mathbf{p}$ depend on the used model, which will be explained later. The matrix $\mathbf{M}$ is typically calculated using training color patches by least-squares regression as

$$\hat{\mathbf{M}} = \arg\min_{\mathbf{M}} \|\mathbf{Q}_t - \mathbf{M}\mathbf{P}_t\|_F^2, \tag{3}$$

where $\|\cdot\|_F^2$ is the Frobenius norm, $\mathbf{Q}_t \in \mathbb{R}^{4 \times K}$ is the matrix containing the target vectors of K training patches, where the target sRGB and NIR spaces were defined in subsection III-B, $\mathbf{P}_t \in \mathbb{R}^{N \times K}$ is the matrix containing the corresponding input vectors formed by the camera RGB values of the patches. In our evaluation, we used the 96 patches of the X-rite SG color chart, as shown in Fig. 2, for training the color correction matrix. We next explain the used LCC [26], PCC, [27] and RPCC [28] models.

2) LCC model: LCC only uses the first-order linear terms. The input camera intensity vector of LCC is formed as $\mathbf{p}_{lcc} = [r, g, b, n]^T$, where r, g, b, and n represent the camera R, G, B, and NIR values, respectively.

3) PCC model: PCC exploits high-order terms, in addition to the linear terms. In this work, we consider the second-order PCC. The input vector of the second-order PCC is formed as $\mathbf{p}_{pcc} = [r, g, b, n, rg, rb, rn, gb, gn, bn, r^2, g^2, b^2, n^2]^T$.

4) RPCC model: RPCC modifies PCC by taking k^{th} root of each k-degree term to improve the robustness in intensity changes. In this work, we consider the second-order RPCC. The input vector of the second-order RPCC is formed as $\mathbf{p} = [r, g, b, n, \sqrt{rg}, \sqrt{rb}, \sqrt{rn}, \sqrt{gb}, \sqrt{gn}, \sqrt{bn}]^T$. We note that the dimension of the RPCC is lower than PCC because $[\sqrt{r^2}, \sqrt{g^2}, \sqrt{b^2}, \sqrt{n^2}]^T = [r, g, b, n]^T$.

5) Performance evaluation: Table III shows the performance comparison of the color correction algorithms. In the table, "No CC" represents the case that no color correction

(a) Demosaicked camera RGB   (b) Color-corrected result by RPCC   (c) Proposed refinement result   (d) Ground-truth sRGB
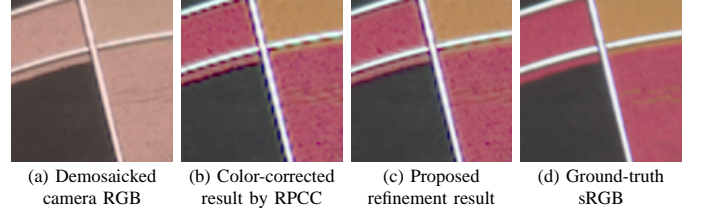
Fig. 8. An example of the demosaicking error amplification for the uniform FAP and the effect of our proposed refinement algorithm: (a) The demosaicked camera RGB image, (b) the color-corrected image by RPCC, (c) the result image after the refinement, and (d) the ground-truth sRGB image.
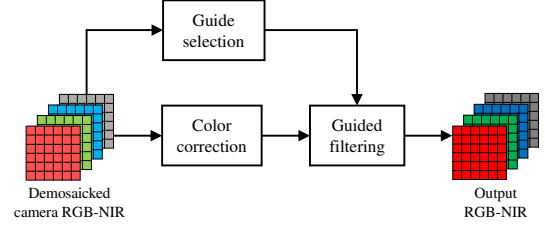

Fig. 9. The flow of our proposed color correction refinement algorithm.

is performed. In terms of the MPSNR performance, we can confirm that the state-of-the-art RPCC consistently offers the best performance for all FAPs. Therefore, In the following experiments, we adopt RPCC.

E. Color correction refinement algorithms

We next address a new challenge of color correction for the RGB-NIR sensors, i.e., demosaicking error amplification, and propose an effective refinement process to suppress the error amplification.

1) Problem statement: One issue of color correction for the RGB-NIR sensors is the amplification of demosaicking errors. Figure 8 shows an example of the error amplification for the uniform FAP, where Fig. 8(a) is the demosaicked camera RGB image and Fig. 8(b) is the color-corrected image by RPCC. It is apparent that the demosaicking errors are severely amplified in the color-corrected image. In the following, we propose an effective color correction refinement algorithm that can suppress the error amplification, as shown in Fig. 8(c).

2) Algorithm flow: Figure 9 shows the flow of our proposed refinement algorithm. Our algorithm is simple and only adds the guided filtering process [48] to the standard color correction process. The guided filtering is a powerful edge-preserving filtering using a guide image that has correlation with the input filtered image. Our idea is that the amplified errors "after" color correction can be filtered out with the guided filtering by using the image "before" the color correction, i.e., before the amplification as the guide. To effectively select the guide channel, we propose two manners as below.

3) Channel-by-channel guided manner: The guide image is selected as channel-by-channel. For example, the color-corrected R image is filtered by using the demosaicked camera R image as the guide. The same process is applied for the other channels.

4) Green guided manner: The demosaicked camera G image is used as the guide for all channels. This manner

TABLE IV
PERFORMANCE EVALUATION OF THE REFINEMENT ALGORITHMS.
AVERAGE PSNR AND MPSNR OF ALL 40 SCENES ARE PRESENTED. THE
BOLD TYPEFACE REPRESENTS THE BEST MPSNR FOR EACH FAP.

FAP	Guide	R	G	B	NIR	MPSNR
Uniform	No refine	29.79	28.94	32.15	27.37	28.85
	Channels	30.79	29.93	32.76	28.00	**29.59**
	Green	30.69	29.93	32.51	28.11	29.56
Dense-NIR	No refine	29.10	32.46	30.80	27.38	29.16
	Channels	30.47	33.56	31.99	28.40	30.22
	Green	30.61	33.56	32.07	28.52	**30.32**
Sparse-NIR	No refine	28.51	32.81	30.33	25.82	28.38
	Channels	29.64	33.44	31.42	26.50	29.19
	Green	29.61	33.44	31.29	26.76	**29.27**

exploits the high sampling density of the G band in the dense-NIR and the sparse-NIR FAPs.

5) Performance evaluation: Table IV presents the performance evaluation of the refinement algorithms. The channel-by-channel manner is slightly better for the uniform FAP. Since the G band is not dominant in the the uniform FAP, the green guided manner is not effective for this FAP. In contrast, the green guided manner works better for the dense-NIR and the sparse-NIR FAPs. These results demonstrate that the high sampling density of the G band can effectively be exploited for the refinement. As a whole, the refinement process improves MPSNR more than 0.7 dB compared with the case without the refinement ("No refine" in the table). In the following experiments, we adopt the best-performed refinement algorithms for each FAP.

F. Optical filter design

We here design an optical filter, which is placed in front of the lens, to improve the RGB-NIR imaging quality. Specifically, we introduce a notch filter as shown in Fig. 10. As can be seen in [21], it is implicitly known that this kind of notch filter can improve the color fidelity of the acquired RGB image. In this work, we explicitly optimize the cutoff wavelengths of the notch filter.

1) Optimization strategy: The definition of the cutoff wavelengths of the simulated notch filter is illustrated in Fig. 10. The curves at the cutoffs are simulated using the sigmoid functions. In the filter optimization, the upper cutoff wavelength is fixed to 800nm according to the assumed target NIR space in subsection III-B (see Fig. 5(d)). Then, we find an optimal notch filter by changing the lower cutoff wavelength.

2) Performance evaluation: Figure 11 shows the MPSNR performance when changing the lower cutoff wavelength of the notch filter. We can see that the cutoff wavelength of 660nm consistently gives the best results for all FAPs. From Fig. 11, in which the results at 800nm correspond to the cases without the notch filter, we can confirm that the notch filter significantly improve the MPSNR performance by optimizing the lower cutoff wavelength.

G. Overall performance summary

In the above subsections, we have investigated the best-performed algorithms for each imaging factor and each FAP.
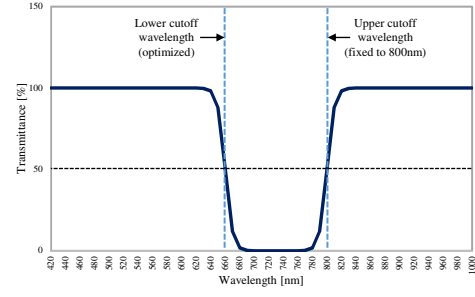

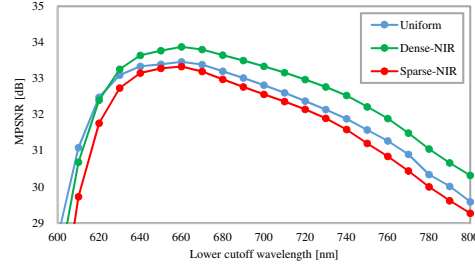Fig. 10. The definition of the cutoff wavelengths of the notch filter.

Fig. 11. MPSNR performance when changing the lower cutoff wavelength of the notch filter. The cutoff at 660nm gives the best results for all FAPs.

TABLE VI
OPERATION MODES OF OUR PROTOTYPE RGB-NIR CAMERA.

Mode	h (pixels)	v (pixels)	bit	fps
1	4096	3072	12	30
2	2816	2816	12	60
3	1984	1984	10	120
4	640	480	12	120
5	640	480	10	300

We here summarize the reported results and compare overall system performance of the considered FAPs. Table V summarizes the step-by-step improvements of the MPSNR performance. We can confirm that each designed step certainly improves the performance. We can also confirm that our proposed dense-NIR FAP presents the best performance when all steps are considered. Figure 12 shows the visual comparison of the result images using the different FAPs. We can confirm that the dense-NIR FAP can generate the images more accurately than the common uniform FAP. Although the MPSNR performance of the sparse-NIR FAP is lowest, the sparse-NIR FAP offers the promising results in the visual comparison.

IV. PROTOTYPE IMPLEMENTATION

A. Configuration

Figure 13 shows the configuration of our developed prototype RGB-NIR camera. We newly developed the RGB-NIR sensor equipped with the RGB-NIR filter array using our dense-NIR FAP. The sensor format is the advanced photo system type-C (APS-C) format. The developed camera system including a field-programmable gate array (FPGA) board, which executes the RGB-NIR imaging pipeline, is placed inside the body of the prototype. The customized notch filter is placed in front of the lens, which modifies the spectral

TABLE V
OVERALL MPSNR PERFORMANCE SUMMARY. THE VALUES IN PARENTHESES REPRESENT THE IMPROVEMENT BY EACH STEP.

FAP	Demosaicked	Color corrected	Refined	Notched
Uniform	17.68	28.85 (+11.17dB)	29.59 (+0.74dB)	33.46 (+3.87dB)
Our dense-NIR	17.69	**29.16** (+11.47dB)	**30.32** (+1.16dB)	**33.88** (+3.56dB)
Our sparse-NIR	**17.70**	28.38 (+10.68dB)	29.27 (+0.89dB)	33.33 (+4.06dB)

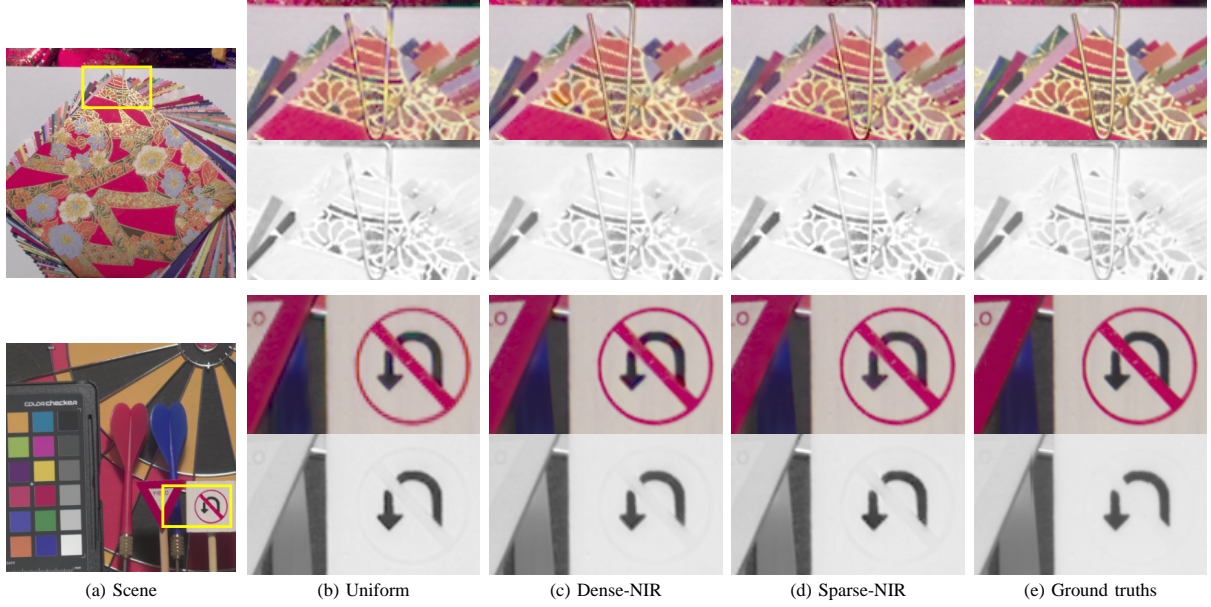(a) Scene (b) Uniform (c) Dense-NIR (d) Sparse-NIR (e) Ground truths

Fig. 12. Visual comparison of the result images using (b) the uniform FAP, (c) the dense-NIR FAP, and (d) the sparse-NIR FAP. For each scene, the upper figures show the RGB images, while the lower figures show the NIR images.
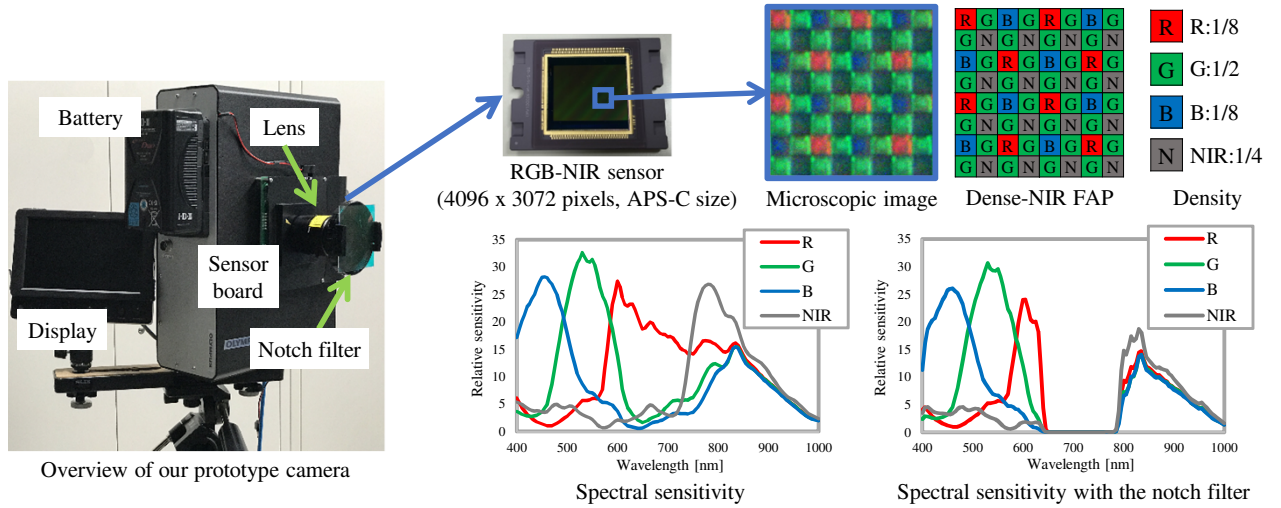

Fig. 13. The configuration of our developed prototype RGB-NIR camera.

sensitivity as shown in the bottom right figure in Fig. 13. The captured RGB and NIR images can be shown side by side through the display in real time. Our prototype camera can be operated in mobile environments using the attached battery and in several operation modes as listed in Table VI. In the highest resolution mode, our prototype camera can capture 4096×3072 RGB and NIR images at 30 frames per second (fps). While in the highest fps mode, our prototype camera can capture 640×480 RGB and NIR images at 300 fps.

B. Potential applications

We demonstrate several potential applications using our prototype camera. Figure 14 shows the RGB and NIR hand images captured by our prototype camera. We can see that our prototype camera can simultaneously capture the standard RGB image and the NIR image, in which the blood vessels are more clearly visible. Figure 15 shows the real and the fake leaves captured by our prototype camera. From the RGB image, it is difficult to recognize which is the real one. In
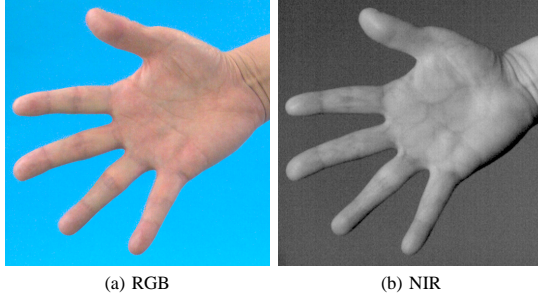
(a) RGB

(b) NIR

Fig. 14. The captured RGB and NIR hand images. The blood vessels are more clearly visible in the NIR image.
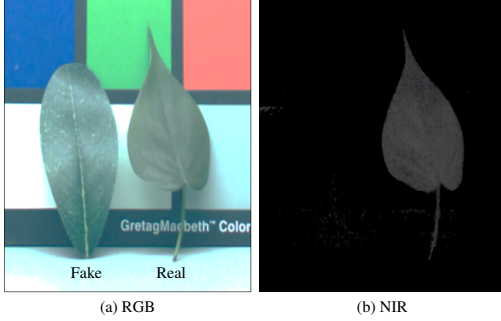

(a) RGB

(b) NIR

Fig. 15. The real and the fake leaves captured by our prototype camera. The real leaf is bright in the NIR image.
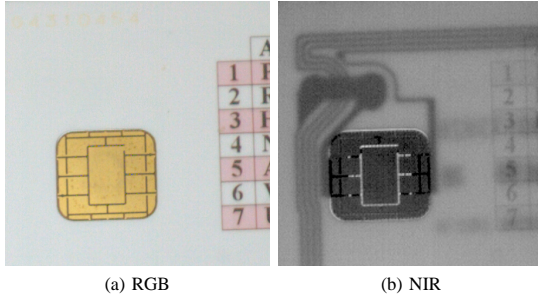

(a) RGB

(b) NIR

Fig. 16. The IC card images captured by our prototype camera. The circuits integrated inside the card are visible in the NIR image, while the numbers on the card are visible in the RGB image.

contrast, we can easily distinguish the real and the fake leaves from the NIR image, in which the real leaf is bright, while the fake leaf is not bright. Figure 16 shows the integrated circuit (IC) card images captured by our prototype camera. We can see that the circuits, which are integrated inside the card, are visible in the NIR image, while the numbers on the card are visible in the RGB image.

We next demonstrate the potential application of our prototype camera for simultaneous acquisition of RGB and NIR florescence images [19], [49]. As a material that emits the NIR fluorescence, we used indocyanine green (ICG), which is used to visualize the location of blood vessels in medical diagnostics. ICG absorbs light around 800nm and emits light around 830nm. Therefore, we used narrow-band NIR light, which has the relative spectral power distribution shown in Fig. 17(a), to excite ICG. To simultaneously acquire the RGB and the NIR fluorescence images, the customized notch filter, which has the transmittance property shown in Fig. 17(b), was placed in front of the lens to cutoff the excitation light and

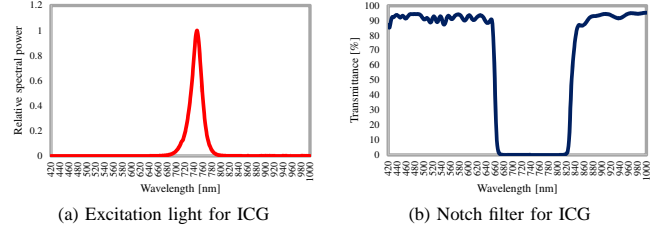(a) Excitation light for ICG

(b) Notch filter for ICG

Fig. 17. The spectral properties of the excitation light and the notch filter used for ICG measurements: (a) The relative spectral power distribution of the excitation light, and (b) the transmittance of the notch filter to cutoff the excitation light and pass the emission light.

(a) RGB

(b) NIR (ICG fluorescence)
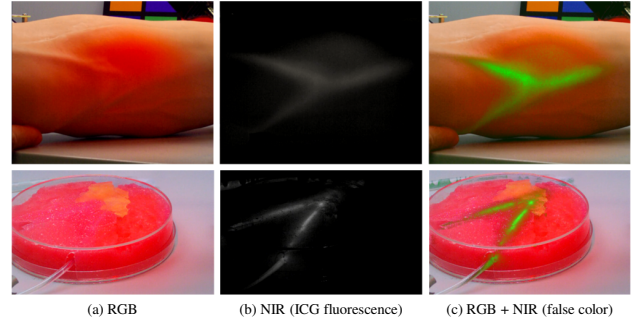
(c) RGB + NIR (false color)

Fig. 18. Simultaneous acquisition of the RGB and the NIR fluorescent images by our prototype camera: (a) The RGB image, (b) the NIR image, which represents the ICG fluorescence, and (c) the visualized RGB+NIR image, where the NIR image is superimposed on the RGB image using the false color. See the text for detailed explanation.

pass the NIR fluorescence light.

In the experiments, we created an arm model and an organ model as shown in Fig. 18. In the models, plastic tubes that simulate blood vessels are located. To simulate blood flows, ICG was circulated in the tubes. Figure 18(a) and 18(b) show the acquired RGB and the NIR fluorescence images by our prototype camera. We can see that our prototype camera can simultaneously capture the RGB image and the NIR image that represents the ICG fluorescence. Because there is no misalignment between the images, we can effectively visualize the location of the tubes (i.e., blood vessels) as shown in Fig. 18(c), where the NIR image is superimposed on the RGB image using the false color.

As demonstrated in the above examples, our prototype RGB-NIR camera has potentials to be used in a wide variety of applications in fields such as medical diagnosis, plant monitoring, and industrial inspection.

V. CONCLUDING REMARKS

In this paper, we have proposed high-quality system designs for single-sensor RGB-NIR imaging. We first have presented a system evaluation framework that takes both the RGB-NIR sensor characteristics and the RGB-NIR imaging pipeline into account. Based on the evaluation framework, we then have designed each imaging factor of the system and have demonstrated that the RGB-NIR imaging quality can be much improved by properly designing each factor. Through the detailed experiments, we have proposed the best-performed system design that is based on our proposed dense-NIR FAP. We finally have presented the configuration of our developed

prototype RGB-NIR camera, which was implemented based on the best-performed system design, and have demonstrated several potential applications using our prototype camera.

Our future work includes the incorporation of denoising and chromatic aberration correction into the RGB-NIR imaging pipeline. Since the noise affects the quality of demosaicking and color correction, we will consider to incorporate an existing raw data denoising method [50] and an effective color correction pipeline with denoising [51]. Chromatic aberration due to a large difference of refraction indexes between RGB and NIR domains is another issue of the single-sensor RGB-NIR imaging. For this issue, we will consider to incorporate recent chromatic aberration correction methods [52]–[55] that are designed for single-sensor RGB-NIR imaging. Smartphone embedded applications [56]–[59] could be one of potential future directions of our RGB-NIR imaging system.

REFERENCES

[1] X. Shen, Q. Yan, L. Xu, L. Ma, and J. Jia, "Multispectral joint image restoration via optimizing a scale map," *IEEE Trans. on Pattern Analysis and Machine Intelligence*, vol. 37, no. 12, pp. 2518–2530, 2015.

[2] E. P. Bennett, J. L. Mason, and L. McMillan, "Multispectral bilateral video fusion," *IEEE Trans. on Image Processing*, vol. 16, no. 5, pp. 1185–1194, 2007.

[3] X. Zhang, T. Sim, and X. Miao, "Enhancing photographs with near infra-red images," *Proc. of IEEE Conf. on Computer Vision and Pattern Recognition (CVPR)*, pp. 1–8, 2008.

[4] D. Sugimura, T. Mikami, H. Yamashita, and T. Hamamoto, "Enhancing color images of extremely low light scenes based on RGB/NIR images acquisition with different exposure times," *IEEE Trans. on Image Processing*, vol. 24, no. 11, pp. 3586–3597, 2015.

[5] D. Connah, M. S. Drew, and G. D. Finlayson, "Spectral edge: Gradient-preserving spectral mapping for image fusion," *Journal of the Optical Society of America A*, vol. 32, no. 12, pp. 2384–2396, 2015.

[6] T. Shibata, M. Tanaka, and M. Okutomi, "Versatile visible and near-infrared image fusion based on high visibility area selection," *Journal of Electronic Imaging*, vol. 25, no. 1, pp. 013 016–1–17, 2016.

[7] L. Schaul, C. Fredembach, and S. Süsstrunk, "Color image dehazing using the near-infrared," *Proc. of IEEE Int. Conf. on Image Processing (ICIP)*, pp. 1629–1632, 2009.

[8] C. Feng, S. Zhuo, X. Zhang, L. Shen, and S. Süsstrunk, "Near-infrared guided color image dehazing," *Proc. of IEEE Int. Conf. on Image Processing (ICIP)*, pp. 2363–2367, 2013.

[9] M. Brown and S. Süsstrunk, "Multi-spectral SIFT for scene category recognition," *Proc. of IEEE Conf. on Computer Vision and Pattern Recognition (CVPR)*, pp. 177–184, 2011.

[10] X. Zhang, T. Sim, and X. Miao, "Not afraid of the dark: NIR-VIS face recognition via cross-spectral hallucination and low-rank embedding," *Proc. of IEEE Conf. on Computer Vision and Pattern Recognition (CVPR)*, pp. 6628–6637, 2017.

[11] D. Rüfenacht, C. Fredembach, and S. Süsstrunk, "Automatic and accurate shadow detection using near-infrared information," *IEEE Trans. on Pattern Analysis and Machine Intelligence*, vol. 36, no. 8, pp. 1672–1678, 2014.

[12] S. Kado, Y. Monno, K. Moriwaki, K. Yoshizaki, M. Tanaka, and M. Okutomi, "Remote heart rate measurement from RGB-NIR video based on spatial and spectral face patch selection," *Proc. of Int. Conf. of the IEEE Engineering in Medicine and Biology Society (EMBC)*, pp. 5676–5680, 2018.

[13] B. Bayer, "Color imaging array," *U.S. Patent 3971065*, 1976.

[14] R. Lukac, *Single-sensor imaging: Methods and applications for digital cameras*. CRC Press, 2008.

[15] B. K. Gunturk, J. Glotzbach, Y. Altunbasak, R. W. Schafer, and R. M. Mersereau, "Demosaicking: Color filter array interpolation," *IEEE Signal Processing Magazine*, vol. 22, no. 1, pp. 44–54, 2005.

[16] X. Li, B. K. Gunturk, and L. Zhang, "Image demosaicing: A systematic survey," *Proc. of SPIE*, vol. 6822, pp. 68 221J–1–15, 2008.

[17] N. Spooren, B. Geelen, K. Tack, A. Lambrechts, M. Jayapala, R. Ginat, Y. David, E. Levi, and Y. Grauer, "RGB-NIR active gated imaging," *Proc. of SPIE*, vol. 9987, pp. 998 704–1–11, 2016.

[18] B. Geelen, N. Spooren, K. Tack, A. Lambrechts, and M. Jayapala, "System-level analysis and design of a compact RGB-NIR CMOS camera," *Proc. of SPIE*, vol. 10110, pp. 101 100B–1–13, 2017.

[19] Z. Chen, X. Wang, and R. Liang, "RGB-NIR multispectral camera," *Optics Express*, vol. 22, no. 5, pp. 4985–4994, 2014.

[20] M. Martinello, A. Wajs, S. Quan, H. Lee, C. Lim, T. Woo, W. Lee, S. S. Kim, and D. Lee, "Dual aperture photography: Image and depth from a mobile camera," *Proc. of IEEE Int. Conf. on Computational Photography (ICCP)*, pp. 1–10, 2015.

[21] H. Tang, X. Zhang, S. Zhuo, F. Chen, K. N. Kutulakos, and L. Shen, "High resolution photography with an RGB-infrared camera," *Proc. of IEEE Int. Conf. on Computational Photography (ICCP)*, pp. 1–10, 2015.

[22] X. Hu, F. Heide, Q. Dai, and G. Wetzstein, "Convolutional sparse coding for RGB+NIR imaging," *IEEE Trans. on Image Processing*, vol. 27, no. 4, pp. 1611–1625, 2018.

[23] K. Kidono and Y. Ninomiya, "Visibility estimation under night-time conditions using a multiband camera," *Proc. of IEEE Intelligent Vehicles Symposium (IV)*, pp. 1013–1018, 2007.

[24] S. Koyama, Y. Inaba, M. Kasano, and T. Murata, "A day and night vision MOS imager with robust photonic-crystal-based RGB-and-IR," *IEEE Trans. on Electron Devices*, vol. 55, no. 3, pp. 754–759, 2008.

[25] D. Kiku, Y. Monno, M. Tanaka, and M. Okutomi, "Beyond color difference: Residual interpolation for color image demosaicking," *IEEE Trans. on Image Processing*, vol. 25, no. 3, pp. 1288–1300, 2016.

[26] P. M. Hubel, J. Holm, G. D. Finlayson, and M. S. Drew, "Matrix calculations for digital photography," *Proc. of Color and Imaging Conference (CIC)*, pp. 105–111, 1997.

[27] G. Hong, M. R. Luo, and P. A. Rhodes, "A study of digital camera colorimetric characterisation based on polynomial modelling," *Color Research and Application*, vol. 26, no. 1, pp. 76–84, 2001.

[28] G. D. Finlayson, M. Mackiewicz, and A. Hurlbert, "Colour correction using root-polynomial regression," *IEEE Trans. on Image Processing*, vol. 24, no. 5, pp. 1460–1470, 2015.

[29] D. Kiku, Y. Monno, M. Tanaka, and M. Okutomi, "Simultaneous capturing of RGB and additional band images using hybrid color filter array," *Proc. of SPIE*, vol. 9023, pp. 90 230V–1–9, 2014.

[30] H. Teranaka, Y. Monno, M. Tanaka, and M. Okutomi, "Single-sensor RGB and NIR image acquisition: Toward optimal performance by taking account of CFA pattern, demosaicking, and color correction," *Proc. of IS&T Electronic Imaging*, pp. DPMI–256–1–6, 2016.

[31] Y. Monno, M. Tanaka, and M. Okutomi, "N-to-sRGB mapping for single-sensor multispectral imaging," *Proc. of Color and Photometry in Computer Vision Workshop (CPCV)*, pp. 66–73, 2015.

[32] T. Nedelcu, S. Thavalengal, and P. Corcoran, "Hybrid visible + near infrared color filter array for handheld consumer imaging applications," *Proc. of IEEE Int. Conf. on Consumer Electronics (ICCE)*, pp. 551–552, 2016.

[33] Y. M. Lu, C. Fredembach, M. Vetterli, and S. Süsstrunk, "Designing color filter arrays for the joint capture of visible and near-infrared images," *Proc. of IEEE Int. Conf. on Image Processing (ICIP)*, pp. 3797–3800, 2009.

[34] Z. Sadeghipoor, Y. M. Lu, and S. Süsstrunk, "Correlation-based joint acquisition and demosaicing of visible and near-infrared images," *Proc. of IEEE Int. Conf. on Image Processing (ICIP)*, pp. 3226–3229, 2011.

[35] ——, "A novel compressive sensing approach to simultaneously acquire color and near-infrared images on a single sensor," *Proc. of IEEE Int. Conf. on Acoustics, Speech and Signal Processing (ICASSP)*, pp. 1646–1650, 2013.

[36] M. Anderson, R. Motta, S. Chandrasekar, and M. Stokes, "Proposal for a standard default color space for the internet - sRGB," *Proc. of Color and Imaging Conference (CIC)*, pp. 238–245, 1996.

[37] H. R. Kang, *Computational color technology*. SPIE Press, 2006.

[38] G. Langfelder, T. Malzbender, A. F. Longoni, and F. Zaraga, "A device and an algorithm for the separation of visible and near infrared signals in a monolithic silicon sensor," *Proc. of SPIE*, vol. 7882, pp. 788 207–1–9, 2011.

[39] C. Park and M. G. Kang, "Color restoration of RGBN multispectral filter array sensor images based on spectral decomposition," *Sensors*, vol. 16, no. 5, pp. 719–1–26, 2016.

[40] Z. Sadeghipoor, J. B. Thomas, and S. Süsstrunk, "Demultiplexing visible and near-infrared information in single-sensor multispectral imaging," *Proc. of Color and Imaging Conference (CIC)*, pp. 76–81, 2016.

[41] C. Aguilera, X. Soria, A. D. Sappa, and R. Toledo, "RGBN multispectral images: A novel color restoration approach," *Proc. of Int. Conf. on Practical Applications of Agents and Multi-Agent Systems (PAAMS)*, pp. 155–163, 2017.

[42] X. Soria, A. D. Sappa, and R. I. Hammoud, "Wide-band color imagery restoration for RGB-NIR single sensor images," *Sensors*, vol. 18, no. 7, pp. 2059–1–17, 2018.

[43] G. Langfelder, "CMOS pixels directly sensitive to both visible and near-infrared radiation," *IEEE Trans. on Electron Devices*, vol. 60, no. 5, pp. 1695–1700, 2013.

[44] B. Geelen, C. Blanch, P. Gonzalez, N. Tack, and A. Lambrechts, "A tiny, VIS-NIR snapshot multispectral camera," *Proc. of SPIE*, vol. 9374, pp. 937 414–1–8, 2015.

[45] J. B. Thomas, P. J. Lapray, P. Gouton, and C. Clerc, "Spectral characterization of a prototype SFA camera for joint visible and NIR acquisition," *Sensors*, vol. 16, no. 7, pp. 993–1–19, 2016.

[46] J. Y. Hardeberg, F. Schmitt, and H. Brettel, "Multispectral color image capture using a liquid crystal tunable filter," *Optical Engineering*, vol. 41, pp. 2532–2548, 2002.

[47] Y. Monno, D. Kiku, S. Kikuchi, M. Tanaka, and M. Okutomi, "Multi-spectral demosaicking with novel guide image generation and residual interpolation," *Proc. of IEEE Int. Conf. on Image Processing (ICIP)*, pp. 645–649, 2014.

[48] K. He, J. Sun, and X. Tang, "Guided image filtering," *IEEE Trans. on Pattern Analysis and Machine Intelligence*, vol. 35, no. 6, pp. 1397–1409, 2013.

[49] V. Venugopal, M. Park, Y. Ashitate, F. Neacsu, F. Kettenring, J. V. Frangioni, S. P. Gangadharan, and S. Gioux, "Design and characterization of an optimized simultaneous color and near-infrared fluorescence rigid endoscopic imaging system," *Journal of Biomedical Optics*, vol. 18, no. 12, pp. 126 018–1–10, 2013.

[50] H. Akiyama, M. Tanaka, and M. Okutomi, "Pseudo four-channel image denoising for noisy CFA raw data," *Proc. of IEEE Int. Conf. on Image Processing (ICIP)*, pp. 4778–4782, 2015.

[51] K. Takahashi, Y. Monno, M. Tanaka, and M. Okutomi, "Effective color correction pipeline for a noisy image," *Proc. of IEEE Int. Conf. on Image Processing (ICIP)*, pp. 4002–4006, 2016.

[52] Z. Sadeghipoor, Y. M. Lu, and S. Süsstrunk, "Gradient-based correction of chromatic aberration in the joint acquisition of color and near-infrared images," *Proc. of SPIE*, vol. 9404, pp. 94 040F–1–11, 2015.

[53] Z. Sadeghipoor, Y. M. Lu, E. Mendez, and S. Süsstrunk, "Multiscale guided deblurring: Chromatic aberration correction in color and near-infrared imaging," *Proc. of European Signal Processing Conf. (EU-SIPCO)*, pp. 2336–2340, 2016.

[54] J. Y. Kwon and M. G. Kang, "Multispectral demosaicking considering out-of-focus problem for red-green-blue-near-infrared image sensors," *Journal of Electronic Imaging*, vol. 25, no. 2, pp. 023 010–1–13, 2016.

[55] M. Helou, Z. Sadeghipoor, and S. Süsstrunk, "Correlation-based deblurring leveraging multispectral chromatic aberration in color and near-infrared joint acquisition," *Proc. of IEEE Int. Conf. on Image Processing (ICIP)*, pp. 1402–1406, 2017.

[56] I. Hussain and P. Nath, "Smartphone-based platform optical setup measuring $\pi/256$ optical phase difference in an interference process," *Applied optics*, vol. 54, no. 18, pp. 5739–5742, 2015.

[57] I. Hussain, K. Ahamad, and P. Nath, "Water turbidity sensing using a smartphone," *RSC Advances*, vol. 6, no. 27, pp. 22 374–22 382, 2016.

[58] P. Edwards, C. Zhang, B. Zhang, X. Hong, V. K. Nagarajan, B. Yu, and Z. Liu, "Smartphone based optical spectrometer for diffusive reflectance spectroscopic measurement of hemoglobin," *Scientific Reports*, vol. 7, no. 1, pp. 12 224–1–7, 2017.

[59] I. Hussain, A. J. Bora, D. Sarma, K. Ahamad, and P. Nath, "Design of a smartphone platform compact optical system operational both in visible and near infrared spectral regime," *IEEE Sensors Journal*, vol. 18, no. 12, pp. 4933–4939, 2018.

Yusuke Monno received the B.E., M.E., and Ph.D degrees from Tokyo Institute of Technology, Tokyo, Japan, in 2010, 2011, and 2014, respectively. He is currently a postdoctoral researcher with the Department of Systems and Control Engineering, School of Engineering, Tokyo Institute of Technology. From Nov. 2013 to Mar. 2014, he joined the Image and Visual Representation Group at Ecole Polytechnique Federale de Lausanne as a research internship student. His research interests are in both theoretical and practical aspects of image processing, computer vision, and biomedical engineering. He received the NF Foundation R&D Encouragement Award in 2015, the Inoue Research Award for Young Scientists and the Seiichi Tejima Doctoral Dissertation Award in 2016, and the IEEE Signal Processing Society Japan Best Paper Award in 2017. He is a member of IEEE.

Hayato Teranaka received the B.E. and M.E. degrees from Tokyo Institute of Technology, Tokyo, Japan, in 2014, and 2016, respectively. He is currently a developer at KONICA MINOLTA, INC., where he is engaged in development of digital image processing at the IoT Service Platform Development Operations. His work focuses on image recognition.

Kazunori Yoshizaki received the B.E., and M.E. degrees from Tokyo University of Agriculture and Technology, Tokyo, Japan, in 1998, and 2000, respectively. He was a Research Engineer at Seiko Epson Corporation from 2000 to 2008. Since 2008, he has been a Senior Supervisor at Olympus Corporation, where he is engaged in research and development in image processing algorithms at the Research and Development Center. His work focuses on multispectral imaging.

Masayuki Tanaka received his bachelor's and master's degrees in control engineering and Ph.D. degree from Tokyo Institute of Technology in 1998, 2000, and 2003, respectively. He was a Software Engineer at Agilent Technology from 2003 to 2004. He was a research Scientist at Tokyo Institute of Technology from 2004 to 2008. He was an Associated Professor at the Graduate School of Science and Engineering, Tokyo Institute of Technology from 2008 to 2016. He was a Visiting Scholar with the Department of Psychology, Stanford University from 2013 to 2014. He was an Associated Professor at the School of Engineering, Tokyo Institute of Technology from 2016 to 2017. Since 2017, he has been a Senior Researcher at National Institute of Advanced Industrial Science and Technology.

Masatoshi Okutomi received the B.Eng. degree from the Department of Mathematical Engineering and Information Physics, University of Tokyo, Tokyo, Japan, in 1981, and the M.Eng. degree from the Department of Control Engineering, Tokyo Institute of Technology, Tokyo, in 1983. He joined the Canon Research Center, Canon Inc., Tokyo, in 1983. From 1987 to 1990, he was a Visiting Research Scientist with the School of Computer Science, Carnegie Mellon University, Pittsburgh, PA, USA. He received the Dr.Eng. degree from the Tokyo Institute of Technology, in 1993, for his research on stereo vision. Since 1994, he has been with the Tokyo Institute of Technology, where he is currently a Professor with the Department of Systems and Control Engineering, School of Engineering.